Flow, Turbulence and Combustion (2024) 112:33–59
https://doi.org/10.1007/s10494-023-00450-1

RESEARCH

Collision Statistics of Droplets in Turbulence Considering Lubrication Interactions, Mobility of Interfaces, and Non-continuum Molecular Effects

Ahmad Ababaei[1] · Antoine Michel[1] · Bogdan Rosa[1,2]

Received: 26 April 2023 / Accepted: 21 June 2023 / Published online: 6 July 2023

Abstract
Collision statistics of same-size aerodynamically interacting droplets in homogeneous isotropic turbulence is examined via hybrid direct numerical simulations combined with Lagrangian particle tracking under a point-particle assumption and a one-way momentum coupling. The simulations are performed both in the absence and presence of gravity for various droplet Stokes numbers (0.1–2) over a wide range of liquid water contents (LWCs = 1–30 g/m^3). Also, the effects of using different representations of the lubrication forces, i.e. a continuum and a non-continuum one, have been investigated. The results have highlighted the importance of considering the aerodynamic interaction, especially in the presence of gravity for the systems that have high LWCs. Likewise, taking the lubrication force into account shows a notable change in statistics, but a non-continuum representation yields results that are close to the continuum one. In addition, the impact of modeling droplets as fluid drops instead of rigid particles has been examined. Obtaining quite close statistics under both cases demonstrates that a rigid particle assumption for water droplets in air is sufficiently accurate owing to the high water-to-air viscosity ratio. Moreover, the collision efficiency is shown to be in the range 60–100% in the absence of gravity, which approaches 100% as the LWC is enlarged. In the presence of gravity, however, the efficiency grows, with both the Stokes number and the LWC, to values as high as 300%. Finally, for settling droplet systems, the enhancement factor due to turbulence is quantified, exhibiting a growth with the LWC and a reduction with the Stokes number.

Keywords Particle-laden turbulence · Aerodynamic interaction · Lubrication · Droplet · DNS

✉ Bogdan Rosa
bogdan_rosa@sggw.edu.pl

[1] Institute of Meteorology and Water Management – National Research Institute, Podleśna 61, 01-673 Warsaw, Poland

[2] Department of Applied Mathematics, Warsaw University of Life Sciences, Nowoursynowska 166, 02-776 Warsaw, Poland

1 Introduction

Turbulence-induced collision–coalescence is an important factor contributing to the growth of water droplets in atmospheric clouds. In particular, turbulence is the main driving mechanism for coalescence of droplets in the size gap (radius $\approx$ 15–40 µm) for which neither diffusion nor accretion due to differential settling are efficient (Grabowski and Wang 2013). For fog droplets or micron-sized particles, Brownian diffusion also has an appreciable effect on the collision rate. However, its contribution quickly declines as the particle inertia (size) increases, becoming negligible for droplet pairs having radii of 10 µm (Chun and Koch 2005; Patra and Roy 2022). These complex microscale processes play a key role in drizzle onset and warm rain initiation (Beard and Ochs 1993). Apart from natural phenomena, there are many technological processes in which particle-laden turbulent flows are present. For example, turbulence is the underlying mechanism for the evolution of droplet size spectrum from high-pressure injectors (Pawar et al. 2015) and influences the collection efficiency of wet-scrubbing depollution systems (Rafidi et al. 2018).

In recent years, numerical simulation has brought notable insight into the contribution of turbulence to the dynamics of small inertial droplets. First and foremost, the turbulent eddies increase the collision rate by decorrelating the relative velocity of droplet pairs (Sundaram and Collins 1997). This increase reaches a maximum for droplets having an inertial relaxation time of the order of large-eddy turnover time, $\tau_p = O(T_e)$, of the flow (Sundaram and Collins 1997; Zhou et al. 1998; Wang et al. 2000). Past this peak, droplets of even higher response times, or equivalently larger inertia, are less responsive to flow solicitations, resulting in a decline in their relative velocity. The second effect induced by turbulence is the so-called preferential concentration. It originates from the non-uniformity of droplet distribution in space. Due to centrifugal force the inertial particles are expelled out of vortical tubes into regions of low vorticity and high strain rate (Maxey 1987b; Squires and Eaton 1990). Sundaram and Collins (1997) quantified this accumulation effect by defining the radial distribution function (RDF) as the enhancement in the droplet pair concentration relative to that of a uniform droplet distribution. Using the value of RDF at contact (enhancement in the concentration of pairs that are almost touching each other), it has been shown that in monodisperse systems preferential concentration also depends on the relaxation time, reaching a peak when this characteristic time is of the order of Kolmogorov time scale, $\tau_p = O(\tau_K)$, of the flow (Sundaram and Collins 1997; Zhou et al. 1998; Reade and Collins 2000). The analysis of these two seemingly independent mechanisms suggests that (i) large-scale turbulent motion enhances the collision rate of droplets by increasing their relative velocity, and (ii) preferential concentration is of equal importance for collisions in systems of like-sized droplets (Ayala et al. 2008). However, there is an interplay between these two effects due to the coexistence of a large number of time and length scales in the turbulent flow. Perrin and Jonker (2014) noted that collisions are more likely to occur in regions where vorticity, as well as dissipation rate, is noticeably higher than that in regions where particles (droplets) prefer to occupy. The reason is the reduction in the relative velocity (lower RRV) due to the enhancement in velocity coherence within clusters (higher RDF). Once clustered, they also demonstrate, local dissipative events, rather than vortical accelerations, decorrelate the relative velocity of nearby droplets, assisting them in running into each other. Preferential sweeping of inertial particles by eddies is another phenomenon induced by turbulence via promoting droplet concentration in downward-moving fluid parcels (Maxey and Corrsin 1986; Maxey 1987a). As a result, the inertial particles have an average settling velocity larger than their terminal

velocity in still fluid (Wang and Maxey 1993; Ayala et al. 2008; Ireland et al. 2016; Rosa et al. 2016). By defining the particle Froude number as the ratio of its inertial response time to its residence time within an eddy, Dávila and Hunt (2001) argued that the largest enhancement in the average settling velocity happens when $\tau_p = O(\sqrt[3]{\nu/g^2})$, where ν and g are the kinematic viscosity of the flow and gravitational acceleration, respectively (Rosa et al. 2016). However, settling velocity does not always increase by turbulence (Fornari et al. 2016; Good et al. 2014). Other mechanisms such as loitering (Nielsen 1993), vortex trapping (Tooby et al. 1977), and nonlinear drag (Fung 1998) can lead to a reduced settling velocity. Turbulence-induced phenomena are not limited to those presented here (Falkovich and Pumir 2007; Grabowski and Wang 2013; Voßkuhle et al. 2014).

Many of the studies mentioned above have relied on direct numerical simulations (DNS) of homogeneous isotropic turbulence (HIT) coupled with Lagrangian particle tracking under a one-way momentum coupling assumption that accounts for fluid–particle interaction. Although the particle–particle aerodynamic interaction (AI) was usually neglected to simplify the models, recent experimental results have highlighted its importance for the motion of particles (Yavuz et al. 2018; Magnusson et al. 2022; Bragg et al. 2022). The complex dynamics resulting from the aerodynamic interaction of the droplets notably alters the collision rate of droplets settling in quiescent (Rother et al. 2022; Ababaei and Rosa 2023) and turbulent flows (Pinsky et al. 2001; Wang et al. 2008; Chen et al. 2018b; Dhanasekaran et al. 2021a). When AI is taken into account, the disturbances induced by the motion of neighboring particles deflect their trajectories from the ones when AI is neglected (see Figs. 6–8 in Wang et al. 2005b). As a consequence, this leads to a change in the collision rate of particles. As such, the collision efficiency can be defined as a measure to quantify the impact of AI on the collision rate (Hall 1980; Pinsky et al. 2001; Wang et al. 2005b). For the simplified case of a pair of unequal droplets settling in quiescent air, the collision efficiency corresponds to a critical horizontal offset. In the literature, the gravitational collision efficiency has been computed by examining various AI force representations, short-range effects, and methodologies (Hocking 1959; Shafrir and Neiburger 1963; Davis and Sartor 1967; Hocking and Jonas 1970; Klett and Davis 1973; Davis 1984; Wang et al. 2005a; Rosa et al. 2011; Rother et al. 2022; Ababaei and Rosa 2023). The results show that AI tends to prevent collisions between like-sized and very-different-sized particles, with even a stronger hindering impact when lubrication effects are accounted for. Investigating the same problem (i.e. two settling droplets) in a turbulent environment has revealed that turbulence increases the collision efficiency (de Almeida 1979; Grover and Pruppacher 1985; Koziol and Leighton 1996; Pinsky et al. 1999, 2001). Not only did these studies make use of ad hoc turbulence models, but they were also limited to pair-wise AI between droplets. Similarly, the pair-wise AI scheme has been employed in a number of studies that solve the background turbulent flow (Brunk et al. 1998; Onishi et al. 2013; Akiki et al. 2017a, b). The pair-wise scheme can accurately handle the AI representation for systems with a small number of droplets. However, the general problem of quantifying the collision efficiency in particle-laden turbulent flows requires a methodology to determine many-body AI among droplets. This is particularly important for modeling systems of a high liquid water content (LWC) that need tracking a large number of mutually interacting droplets.

Several methodologies have been proposed to account for many-body interaction among particles (Durlofsky et al. 1987; Sangani and Mo 1994, 1996; Lefebvre-Lepot et al. 2015). In an attempt to develop a scheme that handles many-body AI, Wang et al. (2005a) formulated an improved superposition method (ISM) based on which an overall perturbation field is obtained by superimposing the disturbance velocities induced by the motion

of particles. This method was coupled with the DNS of the turbulent flow by Ayala et al. (2007), known as hybrid DNS (HDNS), to simulate systems of aerodynamically interacting particles. It has been largely employed to represent AI in several studies focused on cloud microphysics, where collision–coalescence of water droplets is investigated (Wang et al. 2007, 2008, 2009; Chen et al. 2018a). The main limitation of HDNS is that the accuracy of the ISM in predicting the AI forces declines for droplets interacting from distances comparable to or less than their radii (see Figs. 5–7 in Wang et al. 2005a). The inaccuracy stems from the superposition of the Stokes solutions that represent the flow around a single isolated sphere.

Several studies in the literature provide exact solutions to the Stokes flow around two spheres (e.g. Jeffrey and Onishi 1984), also deriving the hydrodynamic force and torque acting on them (see a brief survey of these studies in Appendix A of Ababaei and Rosa 2023). Among these studies, those that have particularly focused on two spheres approaching (or retreating) along their line of centers (e.g. Maude 1961; Haber et al. 1973) predict an infinite growth in the resistance coefficients as the gap between the pair diminishes, i.e. a singular growth of $O(\xi^{-1})$ where ξ is the non-dimensional surface-to-surface distance (gap) between the spheres. This is known as lubrication effect. Although the ISM (hence HDNS) precisely predicts the resistance between pairs interacting from long distances, it is unable to capture the short-range lubrication effect. To take the lubrication interactions into account, the resistances from the exact two-sphere (pair-wise) solutions can be utilized for droplets interacting from short distances, while keeping the same many-body structure of ISM for their long-range interaction. The incorporation of short-range lubrication effect into the HDNS demonstrated a notable influence on the collision statistics of same-size particles (Ababaei et al. 2021).

The majority of solutions to the Stokes equation employed to predict lubrication forces is based on the assumption that the fluid is a continuous medium. However, when the gap between the droplets is comparable to the mean free path of the fluid's molecules, the continuum mechanical theories are no longer valid (Sundararajakumar and Koch 1996; Chun and Koch 2005), and the exact analytical solutions lose their accuracy. At such gaps the discrete molecular character of the fluid, i.e. non-continuum effects, must be considered. This results in lubrication resistance increasing at a logarithmic pace of $O(\ln \ln \xi^{-1})$ as the gap between the particles narrows down (Davis 1984; Patra et al. 2022), leading to lower forces compared with the drag from the continuum solutions. Sundararajakumar and Koch (1996) solved the flows under different non-continuum regimes depending on the size of the gap and provided analytical expressions for pressure distribution and drag force. Dhanasekaran et al. (2021b) fitted a function to these solutions in such a way that it uniformly covers all the regimes by smooth transitions. The complementary resistances for the non-continuum force–torque representation normal to the line of centers of the pair have been recently developed by Li Sing How et al. (2021).

The lubrication forces also differ when the internal circulation of droplets is taken into consideration. Instead of an increase inversely proportional to the gap size derived for spherical rigid particles (RP), it has been shown that the growth in lubrication forces acting on a pair of spherical fluid drops (FD) is of $O(\xi^{-\frac{1}{2}})$, that is inversely proportional to the square root of the gap size (Zinchenko 1978; Davis et al. 1989). Haber et al. (1973) developed the exact solution to two unequal fluid drops having different viscosities and moving with any orientation along their line of centers. An exact solution to the translation of such a pair normal to their line of centers was derived by Zinchenko (1980). Taken together, these two studies yield an exact representation for the forces acting on two fluid drops interacting in a viscous fluid. The significance of these short-range AI effects on the

resistance coefficients as well as the gravitational collision efficiency was recently highlighted (Rother et al. 2022; Ababaei and Rosa 2023).

The aim of this study is to analyze the influence of (i) non-continuum molecular effects as well as (ii) internal circulation of fluid drops on the collision statistics for both non-settling and settling droplet systems within a wide range of liquid water contents (1–30 g/m^3). Since these two effects modify the resistances, the results will be compared with the cases where (iii) lubrication force is computed via the continuum representation, the basic cases where (iv) lubrication is not considered, i.e. standard HDNS, and the cases where (v) AI is neglected, i.e. non-interacting rigid particles and fluid drops. The kinematics (at-contact RRV and RDF) as well as the dynamics (collision kernel and collision efficiency) of these systems will be reported and discussed. Finally, a comparison among the turbulence enhancement factors in settling droplet systems will demonstrate the importance of turbulence relative to that of gravity in boosting the collision rate.

2 Methodology

This section discusses the numerical model employed for computing droplet collision statistics in turbulent air. The details already elaborated in other studies are referred to and only briefly mentioned. The description of the numerical approach for simulating the background flow field is followed by the Lagrangian method for tracking the droplets. The assumptions based on which the droplets have been simulated are presented subsequently. Then we analyze the numerical models used to represent the AI among the droplets and compare these models by evaluating the drag force calculated from each of them. Finally, the definitions are given for the statistical parameters used to quantify the kinematics and dynamics of the modeled systems.

2.1 Simulation of the Background Flow

Using the pseudospectral method (Orszag and Patterson 1972), the three-dimensional incompressible homogeneous isotropic turbulent flow of air is modeled in a cube of size 2π. To improve the performance via parallelization, this domain has been decomposed along the two dimensions normal to gravity (y–z). Efficient techniques have been employed to compute 3D fast Fourier transforms (FFTs) within 2D-decomposed domains (Ayala and Wang 2013; Ayala et al. 2014). The applied FFTs imply periodicity along all spatial directions. A uniform grid of N^3 equally spaced nodes is utilized to discretize the governing equations, i.e. Navier–Stokes and continuity

$$\frac{\partial \boldsymbol{U}}{\partial t} = \boldsymbol{U} \times \boldsymbol{\omega} - \boldsymbol{\nabla}\left(\frac{P}{\rho} + \frac{\boldsymbol{U}^2}{2}\right) + \nu \boldsymbol{\nabla}^2 \boldsymbol{U} + \boldsymbol{f}, \tag{1}$$

$$\boldsymbol{\nabla} \cdot \boldsymbol{U} = 0, \tag{2}$$

where $\boldsymbol{U}(\boldsymbol{x}, t)$, $\boldsymbol{\omega}(\boldsymbol{x}, t)$, and $P(\boldsymbol{x}, t)$ denote the velocity, vorticity, and pressure fields of the flow, respectively. Also, $\rho = 10^{-3}$ g/cm^3 and $\nu = 0.17$ cm^2/s are the density and kinematic viscosity of air, respectively. The external force acting on the flow $\boldsymbol{f}(\boldsymbol{x}, t)$ is the source to maintain a stationary turbulent field by artificially supplying the largest scales of the flow with kinetic energy. To do so, a deterministic forcing scheme, similar to the one by

Sullivan et al. (1994), has been employed in Fourier space to maintain a constant energy level for the first two lowest wavenumber modes. The dissipation rate of kinetic energy for the turbulent flow is set to $\epsilon = 400\ \mathrm{cm}^2/\mathrm{s}^3$. Starting from a random field, the homogeneous isotropic turbulent flow has been developed by integrating the governing equations. At this stage, the droplets have not been added to the domain and the equations are integrated using a large time step size. The same flow has been utilized with various sets of droplets and aerodynamic interaction models. The settings as well as statistics of the flow are given in Table 1. The definitions of symbols listed in Table 1 are as follows: $\eta_\mathrm{K} = (\nu^3/\epsilon)^{\frac{1}{4}}$ and $\tau_\mathrm{K} = (\nu/\epsilon)^{\frac{1}{2}}$ are Kolmogorov microscales, L_f is the integral length scale, T_e is the large-eddy turnover time, u' is the r.m.s. of velocity fluctuations, L_box is the length of the domain, R_λ is the Taylor-microscale flow Reynolds number, CFL is the Courant–Friedrichs–Lewy number (has to be less than 0.3 for stability and accuracy), $k_\mathrm{max}\eta_\mathrm{K}$ is the resolution parameter (kept closer to unity to maximize R_λ), and $\mathcal{S}$ and $\mathcal{F}$ are the skewness and flatness of longitudinal velocity gradient, respectively (Wang and Maxey 1993). In the present study, the physical parameters (R_λ, ϵ, and ν) and the numerical procedure (deterministic forcing scheme, grid resolution) are similar to those employed by Rosa et al. (2013). Thus, the flow statistics presented in Table 1 closely match the values reported therein. The relative error does not exceed 2% which ensures the validity of the HIT flow evolved here.

2.2 Lagrangian Particle Tracking

The particles (droplets) are introduced into the domain at random locations after the flow reaches a statistically stationary state. Initially, each particle has the same velocity as that of the background flow at its location. Terminal velocity is added only when gravitational acceleration is included. Then, their velocities and locations are updated by integrating the equations of motion. Since, the density ratio of water to air is large (~ 1000), the original equations derived by Maxey and Riley (1983) reduce to

$$\frac{\mathrm{d}\boldsymbol{V}^{(i)}}{\mathrm{d}t} = -\frac{\boldsymbol{V}^{(i)} - \left(\boldsymbol{U}^{(i)} + \boldsymbol{u}^{(i)}\right)}{\tau_\mathrm{p}^{(i)}} + \boldsymbol{g}, \tag{3}$$

$$\frac{\mathrm{d}\boldsymbol{Y}^{(i)}}{\mathrm{d}t} = \boldsymbol{V}^{(i)}, \qquad i = 1, \ldots, N_\mathrm{p} \tag{4}$$

in which $\boldsymbol{V}^{(i)}$ and $\boldsymbol{Y}^{(i)}$ are the velocity and location of i-th particle. $\boldsymbol{U}^{(i)} \equiv \boldsymbol{U}(\boldsymbol{Y}^{(i)}, t)$ is the background flow velocity interpolated at the location of particles $\boldsymbol{Y}^{(i)}$. In this study, a six-point Lagrangian scheme (Balachandar and Maxey 1989) is used to interpolate the three components of the velocity field. The AI among the particles is taken into account via $\boldsymbol{u}^{(i)}$ which symbolizes the net disturbance velocity at the location of i-th particle induced by

Table 1 Input parameters and average flow statistics

N^3	$\Delta t \times 10^4$	$\Delta x \times 10$	$\eta_\mathrm{K} \times 10^2$	$\tau_\mathrm{K} \times 10^2$	L_f	$T_\mathrm{e} \times 10$
64^3	4.46 s	1.61 cm	5.92 cm	2.06 s	2.66 cm	4.14 s
u'	L_box	R_λ	CFL	$k_\mathrm{max}\eta_\mathrm{K}$	$\mathcal{S}$	$\mathcal{F}$
12.76 cm/s	10.32 cm	77.12	0.23	1.10	−0.42	4.51

the motion of all particles in its proximity. Accordingly, $\boldsymbol{u}^{(i)} = 0$ when the AI of droplets is neglected. The gravitational acceleration and particle inertial relaxation time are marked by $\boldsymbol{g}$ and $\tau_{\mathrm{p}}^{(i)}$, respectively. The latter is defined as

$$\tau_{\mathrm{p}}^{(i)} \equiv \frac{m}{6\pi\mu a\ \tilde{\mu}_{\mathrm{r}}} = \frac{2}{9}\frac{\rho_{\mathrm{p}} a^2}{\mu\tilde{\mu}_{\mathrm{r}}}, \tag{5}$$

where m and ρ_{p} are the mass and density of the droplet, and $\mu = \rho\nu$ is the dynamic viscosity of air. In general, the inertial response time of the droplets depends on their properties, i.e. the parameters mentioned above except μ. Since only monodisperse systems (consisting of equal-sized droplets) are considered here, the superscript "(i)" will be dropped from now on. The additional factor $\tilde{\mu}_{\mathrm{r}}$ appears due to the Stokes drag exerted by a fluid of viscosity μ on an *isolated* (i.e. non-interacting) spherical fluid drop of viscosity μ_{p} translating at the velocity V (Hadamard–Rybczyński problem; Hadamard 1911; Rybczyński 1911; Batchelor and Batchelor 2000; Kim and Karrila 2013)

$$F_{\mathrm{iso}} = -6\pi\mu a V \underbrace{\frac{\hat{\mu}_{\mathrm{r}} + \frac{2}{3}}{\hat{\mu}_{\mathrm{r}} + 1}}_{\tilde{\mu}_{\mathrm{r}}}. \tag{6}$$

Here, the symbol $\hat{\mu}_{\mathrm{r}}$ stands for the viscosity ratio, namely $\hat{\mu}_{\mathrm{r}} \equiv \mu_{\mathrm{p}}/\mu$. The special case of Stokes drag acting on a rigid sphere is recovered when $\hat{\mu}_{\mathrm{r}} \to \infty$ (Kim and Karrila 2013). The accents indicate that the values are dimensionless.

The equations of motion, Eqs. (3) and (4), are integrated using fourth-order Adams–Moulton and Adams–Bashforth schemes. The time step used in every system for advancing both the flow and droplets is $\Delta t \approx \tau_{\mathrm{p}}/100$, which was shown to yield reliable statistics (Ababaei et al. 2021). After integration at each time step, periodicity is applied to the particles whose new locations fall outside the computational domain; this simply means adding or subtracting the spectral length of the domain box, 2π, to or from their updated locations. When a collision is detected, one droplet from the pair is randomly relocated (Wang et al. 2005b). The properties of droplets in the simulated systems are summarized in Table 2. The size of droplets depends on the Stokes number (measure of their inertia) defined as $St \equiv \tau_{\mathrm{p}}/\tau_{\mathrm{K}}$, being proportional to the square of the droplet radius. The considered range $0.1 \leq St \leq 2$ corresponds to the droplets $10 < a < 60$ µm that move in turbulent flows having a kinetic energy dissipation rate $\epsilon = 400\ \mathrm{cm}^2/\mathrm{s}^3$. Due to the small difference in τ_{p} of rigid particles and fluid drops, two sets of settings have been obtained for systems of droplets having a liquid water content (LWC) of 1 $\mathrm{g/m}^3$. For higher LWCs, the given number of droplets, N_{p}, needs to be multiplied by the LWC.

2.3 Assumptions for Droplets

The approach employed here to compute AI treats "droplets" as either spherical rigid particles (RP) or fluid drops (FD). For fluid drops it has been assumed that the external and internal flow fields are all in Stokes regime. Also, the velocity and tangential stress are continuous at the interfaces, and there is no mass flux through the interfaces. As such, the internal flows of drops are usually referred to as internal circulation. Furthermore, the surface tension, $\sigma = 0.073$ N/m, is high enough to neglect the deformation of drops. The deformability is assessed using the Weber number defined as $We \equiv \rho_{\mathrm{p}} a v^2/\sigma$,

Table 2 Basic properties of the droplet systems with a LWC of 1 g/m^3

St	τ_p (s)	Rigid particles		Fluid drops	
		N_p	a (μm)	N_p	a (μm)
0.1	0.002	130,876	12.56	131,536	12.54
0.2	0.004	46,272	17.76	46,505	17.73
0.3	0.006	25,187	21.75	25,314	21.71
0.4	0.008	16,359	25.12	16,442	25.07
0.6	0.012	8905	30.76	8950	30.71
0.8	0.016	5784	35.52	5813	35.46
0.9	0.019	4847	37.67	4872	37.61
1.0	0.021	4139	39.71	4160	39.65
1.1	0.023	3587	41.65	3605	41.58
1.2	0.025	3148	43.50	3164	43.43
1.4	0.029	2498	46.99	2511	46.91
1.6	0.033	2045	50.23	2055	50.15
1.8	0.037	1714	53.28	1722	53.19
2.0	0.041	1463	56.16	1471	56.07

in which the characteristic velocity can be either the terminal velocity or v_K, leading to a maximum of $We \approx 0.12$ for the largest droplets. Thus, it is assumed that the droplets remain non-deformably spherical. These assumptions have been made when deriving the solution of the Stokes equation to determine the interaction forces. In the current model, the differences between rigid particles and fluid drops are in their inertial relaxation times, Eq. (5), and in their representations of AI forces. For fluid drops, these two factors depend on the viscosity ratio of their internal (water) and external (air) flows. At a temperature close to 0 °C, water and air properties are $\rho_p = 1$ g/cm^3, $\mu_p = 1.67 \times 10^{-2}$ g/cm s, $\rho = 10^{-3}$ g/cm^3, and $\mu = 1.7 \times 10^{-4}$ g/cm s, corresponding to a viscosity ratio $\hat{\mu}_r \approx 100$. This value is used in all simulations where the dispersed phase is represented by fluid drops. Apart from these factors, using the point-particle approach, the rigid particles and fluid drops are treated in the same way. They have the same density (mass) occupying a volume represented by its central point to which the drag forces are applied.

Another important aspect concerns the point-particle approximation. To reduce the computational costs, the droplets are treated as material points. Nonetheless, the finite size of droplets is also considered to detect geometric collisions between them. A droplet radius is attributed to each tracked particle and remains unchanged over the simulation time. Moreover, the rotational motion of rigid particles, induced whether by the background flow or by their interaction with the neighboring particles, is neglected. Both above assumptions are justified since the radii of particles considered here are at least one order of magnitude smaller than the Kolmogorov length scale of the flow (6 mm). Therefore, the smallest vortices are unable to impose substantial torque even on the largest particles (56 μm). Moreover, for fluid drops there is no need to solve an equation for the conservation of angular momentum. Zinchenko (1980) has proved that the hydrodynamic torque acting on fluid drops is always zero.

2.4 Aerodynamic Interaction of Droplets

The AI of droplets is accounted for via the disturbance term $\boldsymbol{u}^{(i)}$ in Eq. (3). Similar to the methodology adopted in Ababaei et al. (2021), the net disturbance of velocity is comprised of

$$\boldsymbol{u}^{(i)} = \boldsymbol{u}^{(i)}_{\mathrm{HDNS}} + \boldsymbol{u}^{(i)}_{\mathrm{SR}}, \tag{7}$$

where the right hand side terms are due to long- and short-range (SR) interactions obtained, respectively, from the hybrid DNS and analytical solutions to the Stokes flow around a pair of spherical drops. In what follows, the approaches to compute each component are presented.

2.4.1 Long-Range Many-Body Interaction Among Droplets

In the limit of low Reynolds number, the disturbance at the location of droplet i induced by a spherical droplet j of radius $a^{(j)}$ and viscosity $\mu_{\mathrm{p}}^{(j)}$ moving at $\boldsymbol{v}^{(j)}$ can be approximated using the analytical solution to the Stokes flow around a single droplet (Hadamard–Rybczyński problem) as follows:

$$\begin{aligned}\boldsymbol{u}_{\mathrm{St}}\left(\boldsymbol{r}^{(ij)};a^{(j)},\boldsymbol{v}^{(j)}\right) = &\left[A_1\frac{a^{(j)}}{r^{(ij)}} - 3B_1\left(\frac{a^{(j)}}{r^{(ij)}}\right)^3\right]\left(\boldsymbol{v}^{(j)}\cdot\hat{\boldsymbol{e}}^{(ij)}\right)\hat{\boldsymbol{e}}^{(ij)}\\ &+\left[A_1\frac{a^{(j)}}{r^{(ij)}} + \ B_1\left(\frac{a^{(j)}}{r^{(ij)}}\right)^3\right]\boldsymbol{v}^{(j)},\end{aligned} \tag{8}$$

where $\hat{\boldsymbol{e}}^{(ij)} = \boldsymbol{r}^{(ij)}/r^{(ij)}$ is the unit vector in radial direction in which $\boldsymbol{r}^{(ij)} \equiv \boldsymbol{Y}^{(i)} - \boldsymbol{Y}^{(j)}$ is the vector connecting centers of droplet j to i, and having the magnitude $r^{(ij)} = \|\boldsymbol{r}^{(ij)}\|$. The factors $A_1 = \frac{2+3\hat{\mu}_{\mathrm{r}}}{4(1+\hat{\mu}_{\mathrm{r}})}$ and $B_1 = \frac{\hat{\mu}_{\mathrm{r}}}{4(1+\hat{\mu}_{\mathrm{r}})}$ have been derived analytically (e.g. in Example 4.3 of Kim and Karrila 2013). We note that in the limit $\hat{\mu}_{\mathrm{r}} \to \infty$, Eq. (8) converges to the formula representing the Stokes disturbance generated by a rigid sphere translating in a viscous fluid (Exercise 2.7 in Kim and Karrila 2013). Accordingly, by utilizing Eq. (8) instead of Stokes disturbance field of a rigid sphere, the improved superposition method (ISM) of Wang et al. (2005a) can be generalized for spherical fluid drops.

Furthermore, using Eq. (8) in the hybrid DNS (HDNS) approach (Wang et al. 2005a; Ayala et al. 2007), the net disturbance at the location of every droplet can be evaluated by superposing the Stokes disturbances of all neighboring droplets as follows:

$$\boldsymbol{u}^{(i)}_{\mathrm{HDNS}} = \sum_{\substack{j=1\\ j\neq i}}^{N_{\mathrm{p}}} \boldsymbol{u}_{\mathrm{St}}\left(\boldsymbol{r}^{(ij)};a^{(j)},\boldsymbol{V}^{(j)} - \left(\boldsymbol{U}^{(j)} + \boldsymbol{u}^{(j)}_{\mathrm{HDNS}}\right)\right), \qquad i = 1,\ldots,N_{\mathrm{p}} \tag{9}$$

which results in a linear system of $3N_{\mathrm{p}}$ equations for the three components of disturbance velocity along every spatial direction of each droplet. The disturbance vanishes as the distance from a translating droplet increases: $\boldsymbol{u} \to 0$ when $r^{(ij)} \gg a^{(j)}$. Thus, the net disturbance in Eq. (9) can be computed by superposing only the effective disturbances of neighboring droplets. To exclude the droplets that are too far to have a noticeable contribution to the velocity perturbation, a truncation distance is defined as $\tilde{r}_{\mathrm{tr}} \cdot a^{(j)}$. Ayala et al.

(2007) have shown that the results would not depend on the truncation distance if the factor $\tilde{r}_{\mathrm{tr}} \geq 30$. Still, a more conservative choice, $\tilde{r}_{\mathrm{tr}} = 50$, is made in the present study. This cut-off of ineffective disturbances in Eq. (9) leads to sparse systems of equations which are efficiently solved using a parallel preconditioned solver based on generalized minimal residual (GMRES) method (Torres et al. 2013).

2.4.2 Short-Range Pair-Wise Interaction Between Rigid Particles

Assuming that the droplets are spherical rigid particles (RP), the drag forces acting on pairs can be calculated from the exact analytical solutions. The problem of two rigid spheres translating in a viscous flow at low Reynolds numbers has been analyzed in several studies (Stimson and Jeffery 1926; Maude 1961; O'Neill and Majumdar 1970; Jeffrey and Onishi 1984). Here, we use the standard formulation of the resistance problem

$$\begin{pmatrix} \boldsymbol{u}_{\mathrm{SR}}^{(i)} \\ \boldsymbol{u}_{\mathrm{SR}}^{(j)} \end{pmatrix} = \begin{bmatrix} \boldsymbol{A}_{11} & \boldsymbol{A}_{12} \\ \boldsymbol{A}_{21} & \boldsymbol{A}_{22} \end{bmatrix} \begin{pmatrix} \boldsymbol{V}^{(i)} - \boldsymbol{U}^{(i)} \\ \boldsymbol{V}^{(j)} - \boldsymbol{U}^{(j)} \end{pmatrix}, \tag{10}$$

where each tensor in the resistance matrix, $\boldsymbol{A}_{\alpha\beta}$, is composed of two resistance functions $X^{\boldsymbol{A}}_{\alpha\beta}(s,\lambda)$ and $Y^{\boldsymbol{A}}_{\alpha\beta}(s,\lambda)$ that yield the drag along and normal to the line of centers, respectively. Note that $(\alpha,\beta) \in \{1,2\}$ are the indices of resistance functions whereas $(i,j) \in \{1,\ldots,N_{\mathrm{p}}\}$ identify the pair interacting from a short distance such that $(i,j) \leftarrow (1,2)$. Normalized by $-3\pi\mu(a_\alpha + a_\beta)$, these resistance functions depend only on the normalized separation distance of the pair $s = r/\frac{1}{2}(a_1 + a_2)$ and their radius ratio $\lambda = a_2/a_1$. Since monodisperse systems are being examined here, $s = r/a$ and $\lambda = 1$.

The calculation of resistance functions is quite time-consuming. These functions have to be obtained from infinite series whose terms require computation of remarkably fast-growing coefficients with factors that have complex recurrence relations. Accordingly, calculating and adding enough number of terms for these summations to converge would need large memory allocations as well as considerable numbers of operations. Moreover, doing so for all pairs interacting from short distances at every time step of simulations would be rather inefficient. Therefore, they are tabulated once at the beginning of every simulation. Then, for every interaction with arbitrary values of separation distance, s, the functions are interpolated using a four-point polynomial interpolation (Press et al. 1992).

2.4.3 Short-Range Pair-Wise Interaction Between Fluid Drops

Short-range interaction forces discussed above apply only to rigid particles. Accurate analytical solutions suitable for representing interaction of fluid drops are also available in the literature (Wacholder and Weihs 1972; Haber et al. 1973; Beshkov et al. 1978; Zinchenko 1980; Grashchenkov 1996; Rother et al. 2022). Here, the drag acting on the fluid drops is computed using an approach akin to that given by Eq. (10). The difference is that the resistance coefficients are calculated with considering the internal circulation of the water in the droplets. These solutions for a pair of fluid drops moving along and perpendicular to their line centers are in Haber et al. (1973) and Zinchenko (1980), respectively. Unlike resistances for rigid particles, those of fluid drops depend not only on the separation distance and particle radii but also on the viscosity ratio. Moreover, the inertial relaxation time of fluid droplets, Eq. (5), is larger than that of rigid particles; hence, the terminal velocity is larger, and it takes more time to reach it.

2.4.4 Short-Range Pair-Wise Interaction Between Rigid Particles with Non-Continuum Effects

The force representations described above were based on the analytical solutions to the Stokes equation when treating the ambient flow as a continuous medium. However, when modeling the collisions of cloud droplets, such a simplification is not sufficient if the distance between the droplet surfaces (gap) is comparable with or smaller than the mean free path of the fluid molecules. In this study, the effect of non-continuum interactions is taken into account by modifying the resistance coefficients for rigid particles (Dhanasekaran et al. 2021b). The employed model considers non-continuum lubrication only for the squeezing flow, i.e. a pair of particles approaching each other. Consistent with previous formulations, the non-continuum lubrication forces are represented through the resistance functions

$$X_{11}^{\mathrm{nc}} = X_{11}^{A} + g_1(\lambda)\left(\frac{f^{\mathrm{nc}}}{Kn} - \frac{1}{\xi}\right), \tag{11}$$

$$X_{12}^{\mathrm{nc}} = X_{12}^{A} - \frac{2}{1+\lambda} g_1(\lambda)\left(\frac{f^{\mathrm{nc}}}{Kn} - \frac{1}{\xi}\right), \tag{12}$$

where $Kn \equiv l_{\mathrm{m}}/a$ is the Knudsen number in which $l_{\mathrm{m}}(\approx 0.1\ \mu\mathrm{m}$ for air) is the mean free path of molecules, and $\xi \equiv h/a$ is the gap between droplet surfaces normalized by droplet radius. The function f^{nc} is a smooth fit (given by Dhanasekaran et al. 2021b) to the non-continuum solution developed by Sundararajakumar and Koch (1996), and the function $g_1(\lambda) = 2\lambda^2/(1+\lambda)^3$ is the same as that in Jeffrey and Onishi (1984). It is noteworthy that these resistances converge to the continuum ones (i.e. $X_{\alpha\beta}^{A}$ in Jeffrey and Onishi 1984) at large separation distances. Also, note that the tangential mobilities for shearing flow remain finite at contact (Dhanasekaran et al. 2021b), and the impact of continuum breakdown is less important (negligible for $\xi > 10^{-1}$ when $Kn = 10^{-2}$, Li Sing How et al. 2021).

2.5 Comparison of the Force Representations

The models for droplet AI discussed above are compared with each other. Figure 1 shows the resistance coefficient for a pair of equal spherical droplets (particles) when they move at the same velocity in opposite directions along their line of centers as a function of the normalized gap between them. Both axes are plotted in logarithmic scale. A gap of size $h = a$ divides the whole range of AI into short- and long-range interaction. The representation of long-range interaction is the same under all the models considered, whereas short-range interaction varies depending on the model. The ISM is unable to capture the lubrication effect, i.e. large increase in the resistance, that is observed from the exact analytical solutions. For water droplets in air, the continuum lubrication is almost the same whether the droplets are assumed to be rigid particles (black solid line) or fluid drops (blue solid line). Furthermore, our earlier study on a pair of droplets settling under gravity in quiescent air (Ababaei and Rosa 2023) has revealed that gravitational collision efficiency of droplets differs under RP and FD models. However, these results were obtained for binary droplet systems settling in a quiescent fluid. Additional investigation is needed to confirm such trends in HIT. Compared with the continuum lubrication (CL), when non-continuum effects in the gap between the droplets are taken into

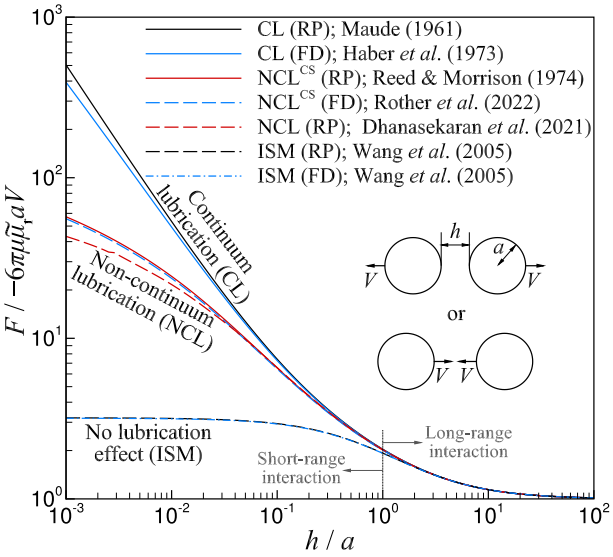

Fig. 1 The resistance coefficients for a pair of spherical droplets moving with the same velocity but in opposite directions along their line of centers as a function of the normalized gap between them. The three lines that represent non-continuum lubrication (NCL) are plotted for droplets of $a = 10$ μm ($Kn = 10^{-2}$). CS stands for continuum–slip

consideration, the short-range force representation exhibits a significant reduction in the resistance. Similar to the CL, the NCL force representations under the slip regime (CS) are almost identical whether droplets are treated as rigid particles or fluid drops (red solid line vs. blue dashed line). The NCL of Dhanasekaran et al. (2021b), red dashed line, assumes Maxwell slip for separations much larger than the mean free path of molecules. Therefore, all the three NCL representations are identical for a gap $h/a \geq 10^{-1}$. For smaller gap sizes, Dhanasekaran et al. (2021b) consider different non-continuum regimes and use their corresponding solutions to obtain the drag. That is why the NCL resistance is slightly lower than the resistances obtained under CS regime.

2.6 Collision Statistical Parameters

The kinematic and dynamic properties of the dispersed flows are quantified in terms of several statistical indices. Due to the large amount of data, the parameters are calculated on-the-fly and recorded at every time step. Averaging over time is performed at the post-processing stage. The first statistical parameter describing kinematics of the modeled systems is the radial relative velocity (RRV). This quantity is a function of the distance between droplets and is defined as

$$\langle |w_r(\hat{r})| \rangle = \frac{1}{c_w(\hat{r})} \frac{1}{n_{\text{pair}}(\hat{r})} \sum_{n=1}^{n_{\text{pair}}} \left| \left(\boldsymbol{V}^{(i)} - \boldsymbol{V}^{(j)} \right) \cdot \hat{\boldsymbol{e}}^{(ij)} \right|. \tag{13}$$

The averaging extends to all the pairs separated by $\hat{r}$, where $\hat{r} \equiv r^{(ij)}/R$ is the center-to-center distance normalized by the collision radius $R = a^{(i)} + a^{(j)} = 2a$. In the numerical implementation, $\hat{r}$ takes discrete values such that the range $1 \leq \hat{r} \leq 10$ is divided into 180 bins corresponding to spherical shells of thickness $\Delta\hat{r} = 0.05R = 0.1a$, as in Rosa et al. (2013). The unit vector in radial direction is $\hat{\boldsymbol{e}}^{(ij)} = \boldsymbol{r}^{(ij)}/r^{(ij)}$. The correction factor $c_w < 1$ accounts for the underestimation in RRV due to the condition of "non-overlapping droplets" imposed by the model. After collisions, one of the droplets is randomly relocated,

creating a droplet-free zone behind the collision sphere. This causes an imbalance in droplet flux through the spherical shells, including the collision sphere. To recover the correct values, Wang et al. (2005b) suggested to remove these flux reductions via dividing the values by analytically derived correction factors which are obtained by subtracting the the flux through the fraction of the area of each shell that is in the shadow of the collision sphere.

The second parameter used to quantify kinematic statistics is the radial distribution function (RDF). This parameter is also a function of the separation distance and is defined as

$$g_{\mathrm{r}}(\hat{r}) = \frac{1}{c_g(\hat{r})} \frac{n_{\mathrm{pair}}(\hat{r})/V_{\mathrm{shell}}(\hat{r})}{N_{\mathrm{pair}}/V_{\mathrm{box}}}, \tag{14}$$

in which $N_{\mathrm{pair}} = \frac{1}{2}N_{\mathrm{p}}(N_{\mathrm{p}} - 1)$ is the total number of pairs, $V_{\mathrm{box}} = L_{\mathrm{box}}^3$ is the volume of the domain, and V_{shell} is the volume of spherical shells having n_{pair} number of pairs between their inner and outer radii of $\hat{r}$ and $\hat{r} + \Delta\hat{r}$, respectively. The kinematic correction factor $c_g < 1$ is due to the non-overlapping droplets condition applied after collisions. The RDF is a measure of clustering in the distribution of droplets in the domain at different length scales. Since it is formulated to be per overall pair number density ($N_{\mathrm{pair}}/V_{\mathrm{box}}$), a value of $g_{\mathrm{r}} = 1$ indicates a uniform distribution.

Computing and recording the collision statistics begins when the system reaches a statistically stationary state. The average volumetric rate of collisions in the domain is called the collision kernel. The kinematic formulation for the collision kernel, $\Gamma^{\mathrm{K}} = 2\pi R^2 \langle |w_{\mathrm{r}}(1)| \rangle g_{\mathrm{r}}(1)$, represents the average flux of droplets through the collision sphere. This quantity is proportional to the two kinematic parameters RRV and RDF at contact, i.e. at the collision radius $r = R$ or $\hat{r} = 1$. The kinematic description of collision kernel was originally proposed by Saffman and Turner (1956), who provided two formulations, a cylindrical and a spherical, to develop a parameterization for the influence of the RRV on the collision rate of inertialess droplets. A careful examination by Wang et al. (1998b) revealed that, even though both formulations are equivalent for gravitational collision rates, only the spherical one is applicable to turbulent flows provided that the particles overlap after collisions. Later, the cylindrical formulation was corrected by Wang et al. (2005c). Also, the corrections when the droplets are not allowed to overlap (e.g. when they interact or when they coalesce into a larger droplet after collisions) were developed by Wang et al. (2005b). These corrections were validated against the dynamic formulation which is based on counting the collisions. Another step in the evolution of the kinematic formulation was to extend it for inertial droplets. This was carried out by Sundaram and Collins (1997) who quantified the clustering in droplet distribution by introducing the RDF at contact, $g_{\mathrm{r}}(1)$, and including it as an enhancement factor in the kinematic formulation. In the current model, the collision events are recorded, allowing us to compute the collision kernel based on the dynamic formulation

$$\Gamma^{\mathrm{D}} = \frac{\dot{N}_{\mathrm{col}}}{N_{\mathrm{pair}}/V_{\mathrm{box}}}, \tag{15}$$

representing the average collision rate per pair number density. The collision rate is computed by counting the collision events N_{col} during the simulation. Collisions are recorded once the distance between a pair is less than the sum of their radii, $r < R$. The details of numerical implementation are described by Wang et al. (1998a). Although the kinematic and dynamic descriptions are equivalent, the dynamic formulation is preferred as it offers

a lower uncertainty and there is no need for corrections. Knowing the collision kernels for both aerodynamically non-interacting and interacting droplet systems, it is possible to estimate the collision efficiency (Wang et al. 2005b)

$$E = \frac{\Gamma^{\mathrm{D}}_{\mathrm{AI}}}{\Gamma^{\mathrm{D}}_{\mathrm{No\ AI}}}. \tag{16}$$

It is noteworthy that the droplets are always relocated after collisions, even in the non-interacting (No AI) systems. This guarantees a realistic evaluation of collision efficiency.

In the studies that examine the collision efficiency of settling droplets in turbulence (e.g. Wang et al. 2008), the enhancement factor in the collision efficiency due to turbulence is defined as (Wang et al. 2005b)

$$\eta_E = \frac{E}{E^g}, \tag{17}$$

where E^g is the gravitational collision efficiency of a pair of droplets settling under gravity in quiescent air. Since E^g cannot be quantified for equal-sized pairs of droplets (due to having the same terminal velocity), the enhancement factor has so far only been computed for bidisperse droplet systems (Wang et al. 2008; Chen et al. 2018a). For the monodisperse systems considered in this study, the quiescent-air collision efficiency has been approximated as $E^g \approx E^g_{12}(\lambda \to 1)$. To do so, the same algorithm in Ababaei and Rosa (2023) was employed using the AI models described above for droplets of sizes given in Table 2 and a radius ratio $\lambda = 0.99$.

3 Results

The inclusion of AI in the model makes the properties of simulated flows sensitive to the liquid water content. That is why the analysis is conducted for droplet systems with different LWCs in range 1–30 g/m^3. Although in typical clouds the LWC is of the order of 1 g/m^3, we have considered a range of higher LWCs to determine the sensitivity of the collision statistics to AI.

In Figs. 2, 3, 4, 5, the left columns show the data obtained from simulations in the absence of gravity. Correspondingly, the results from simulations with the gravitational settling are shown in the panels on the right. The figures in every row provide the results computed using the same LWC under various AI representations. The vertical axis in each figure (set of panels) refers to one of the statistical parameters defined above. All the parameters are a function of the Stokes number.

To the best of our knowledge, this study is original and fills the gap in the existing literature. The unavailability of reference data makes it rather difficult to benchmark our results. Earlier studies that were focused on monodisperse systems disregarded AI (e.g. Sundaram and Collins 1997; Wang et al. 2000; Woittiez et al. 2009; Rosa et al. 2013). In turn, those that considered AI were usually conducted on bidisperse systems (e.g. Koziol and Leighton 1996; Pinsky et al. 1999; Zhou et al. 2001; Pinsky et al. 2007; Wang et al. 2008; Chen et al. 2018a). In addition, the differences in other parameters/settings, such as R_λ and LWC, and numerical approaches utilized make the comparison not fully objective. However, some of the data from recent studies on bidisperse systems (Wang et al. 2008; Chen et al. 2018a) can be used for validation.

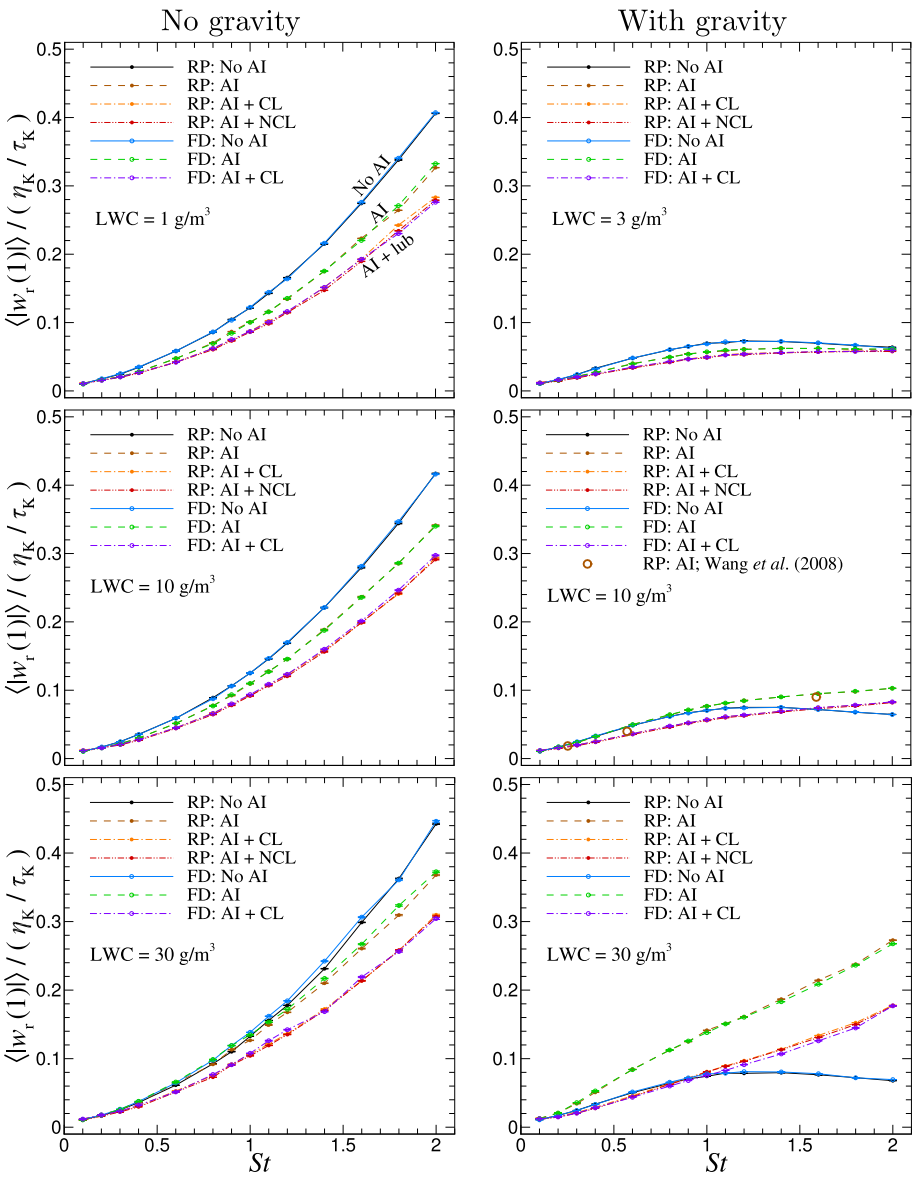

Fig. 2 RRV normalized by Kolmogorov scales of the flow as a function of droplet Stokes number (inertia) under various AI models. Each row of panels corresponds to different LWC

In order to minimize the statistical uncertainties, the simulations were run for quite long times, $O(10^3-10^4\tau_p)$, significantly exceeding $20T_e$. The most challenging cases were those with low-inertia droplets. Simulating systems with small droplets requires utilizing shorter time step sizes, Δt. Hence, a longer simulation time (larger number of time steps, n_t) is needed to record statistics, e.g. collision events, so as to have the same level of uncertainty. Besides, the motion of low-inertia droplets is strongly correlated with the turbulent flow.

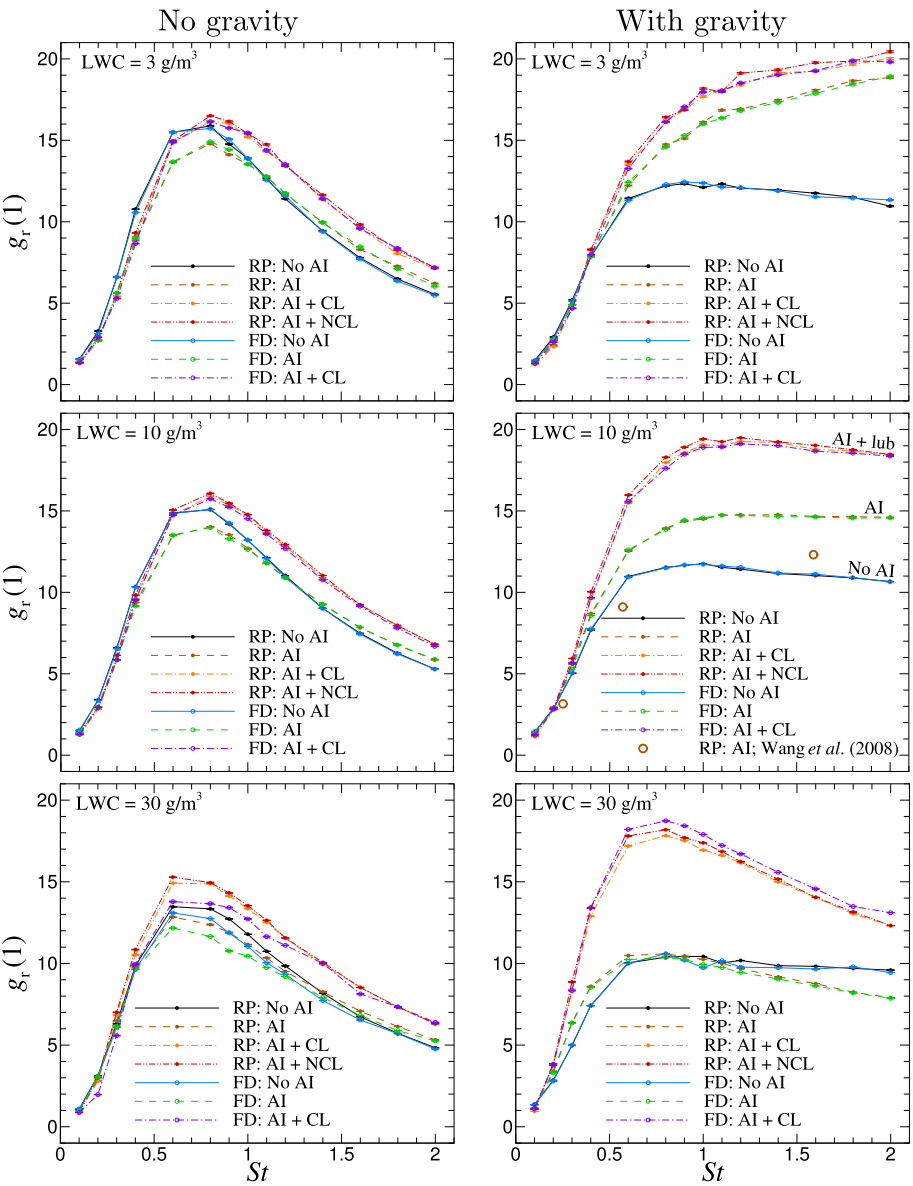

Fig. 3 The RDF as a function of droplet Stokes number under different AI models

This makes them less willing to cluster or collide. As a result, there are a fewer number of samples to compute the statistical parameters at contact. Moreover, minimizing the statistical uncertainties is particularly demanding for systems with very low and very high LWCs. Although modeling low-LWC systems is faster, the smaller number of collisions urges a longer simulation time to collect more samples. On the other hand, the wall-clock time is longer when modeling high-LWC systems. The larger the number of droplets, the longer the wall-clock time it takes to perform droplet-related operations such as building

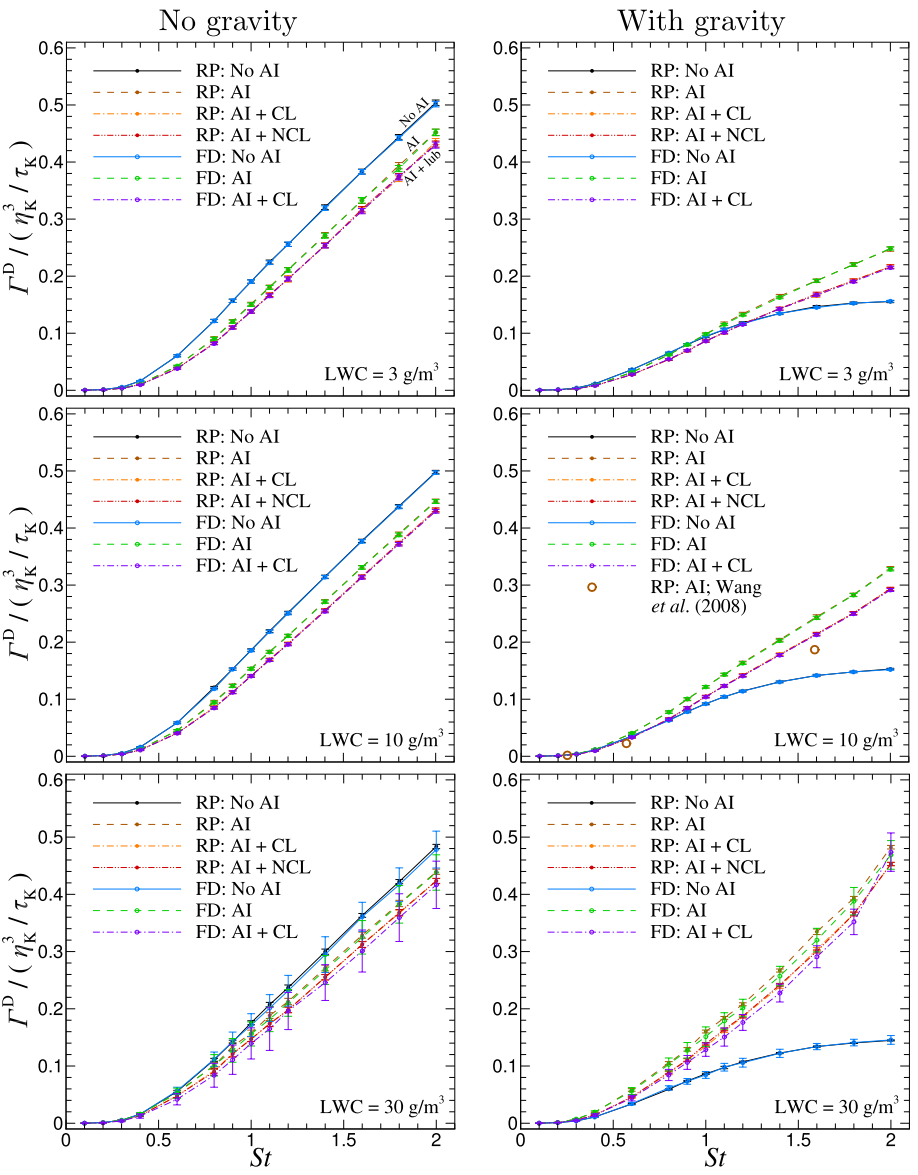

Fig. 4 The dynamic collision kernel, normalized by Kolmogorov scales of the flow, as a function of droplet Stokes number

and solving the system of equations for AI (Eq. (9)), computing short-range AI (Eq. (10)), applying periodicity, relocating particles after collision, and collecting statistical samples for Eqs. (13)–(15).

Figure 2 shows the average radial relative velocity (RRV) of droplets at contact, as a function of Stokes number under various models for representing AI. The RRV is normalized by the Kolmogorov microscales of the turbulent flow. In the absence of gravity, droplet

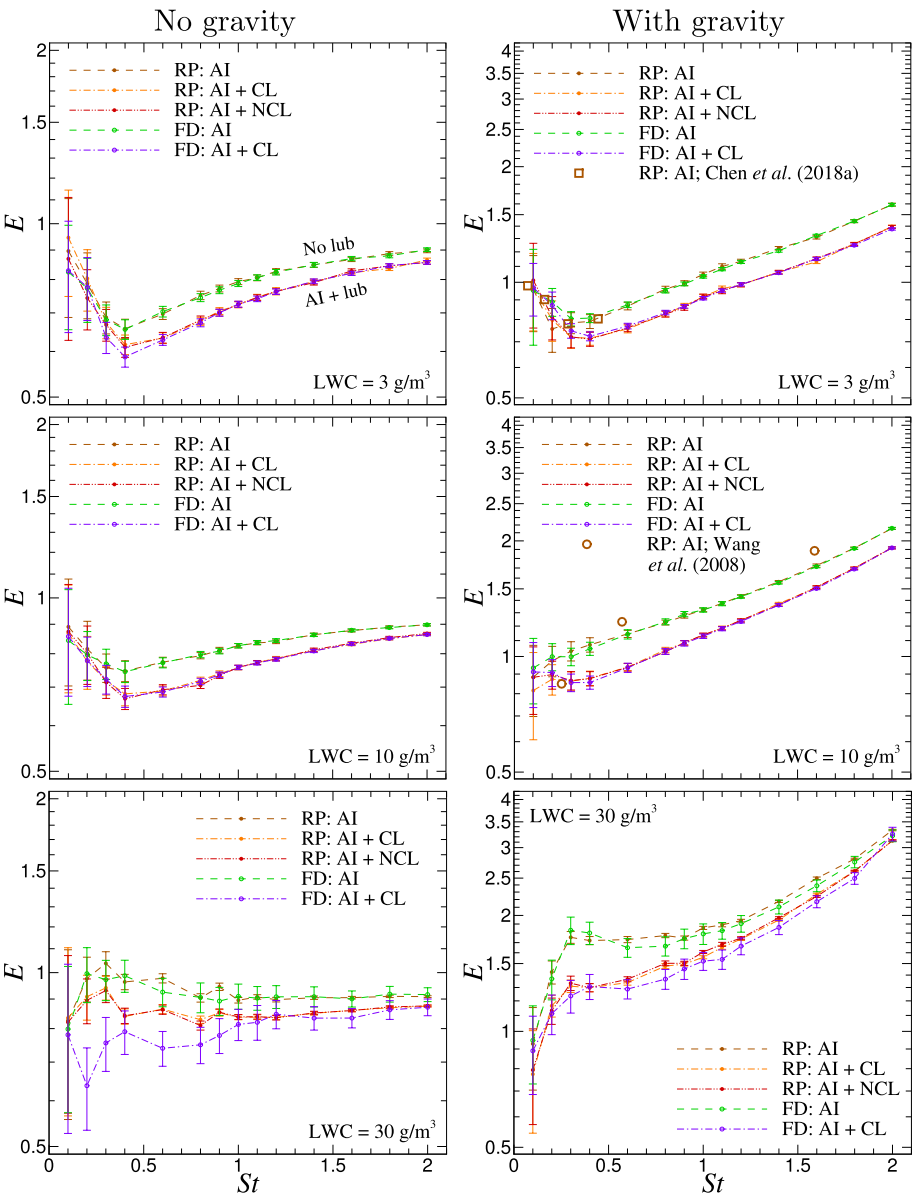

Fig. 5 The collision efficiency as a function of droplet Stokes number

systems exhibit an increase in RRV with the Stokes number. The reason is that the motion of droplets of higher inertia (larger size) is less correlated with the background turbulent flow. Also, there is a slight increase in the RRV of droplets with the LWC. In contrast to dilute systems, the droplets are more densely packed when the LWC is high; hence, the mean distance between them, $(V_{\text{box}}/N_{\text{p}})^{\frac{1}{3}}$, is shorter. As a consequence, droplets are more likely to find each other before viscous drag reduces their velocities. The models employed

to represent AI show three general trends. The largest RRV is when AI is not considered. A reduction in the RRV is observed when AI is represented via HDNS, followed by a further decline when lubrication effect is additionally included. These reductions are due to the resistance between the droplets, which is even stronger when lubrication is accounted for. In the presence of gravity in Fig. 2, the RRV for low-inertia droplets of $St < 0.5$ is similar to the cases when gravity is neglected. At higher St, nonetheless, the RRV is lower compared with non-settling droplets because the gravitational settling diminishes the turbulence effects by reducing the time that droplets interact with eddies (Ayala et al. 2008; Woittiez et al. 2009). In particular, when AI is neglected, there is an enhancement in the RRV of settling droplets of $St \leq 1.2$ for all the LWCs. However, the RRV demonstrates a slight reduction for larger St. Although further enhancement in the RRV is expected at higher inertia, the competing effect of gravitational settling begins to dominate, reducing the droplet–eddy interaction time. This is because heavier droplets attain a terminal velocity larger than the fluctuations of the turbulent flow (Ayala et al. 2008).

In Fig. 2, the mid-right panel (LWC = 10 g/m^3) shows three additional data points taken from Table A.2 of Wang et al. (2008) for RRVs between same-size droplets of radii 20, 30, and 50 μm in a turbulent flow characterized by $R_\lambda = 72.4$ and $\epsilon = 400$ cm^2/s^3. Note that their data were obtained for bidisperse systems; hence, those with the highest droplet radius ratio are taken for comparison here. Also, in their simulations the LWC slightly changed between cases and was roughly of the order of 10 g/m^3. Despite these differences there is a good agreement between the two studies. An interesting observation is that for aerodynamically interacting droplets, there is an increase in the RRV of settling droplets with the LWC. This enhancement stems from the fluctuating disturbance velocity induced by the net far-field many-body interaction of neighboring droplets (see Figure 5 in Wang et al. 2008). As such, this effect (i) is strengthened at higher LWCs, and (ii) does not depend on the background turbulence; hence it is not observed for non-interacting droplets.

For the settling droplets (Fig. 2), analogous to the no-gravity case, including effects of lubrication leads to a decline in the RRV. Another important observation is that the difference between the models that assume droplets as rigid particles and as fluid drops is negligible under all three representations of AI (i.e. no AI, with AI, and with AI plus lubrication). Likewise, non-continuum lubrication has the same influence on the RRV of droplets as continuum lubrication. These observations indicate that, while long-range AI and short-range lubrication effects must be considered in DNS models, taking water droplets (in air) as rigid particles and ignoring non-continuum effects (in the droplet size range analyzed here) are safe assumptions.

An analogous analysis as for the RRV can be performed for the RDF. Figure 3 presents RDF at contact ($\hat{r} = 1$) for the same modeled systems. In the absence of gravity (left panels), the RDF first rises with the Stokes number and then begins to diminish. The RDF of non-interacting droplet systems with LWCs ≤ 10 g/m^3 reaches its peak at a slightly lower Stokes number, i.e. ≈ 0.7, compared to ≈ 0.8 for interacting droplets. Furthermore, AI leads to a reduction in clustering especially in the range $0.5 < St < 1$. Conversely, AI with lubrication forces enhances at-contact pair concentration especially at larger LWCs. As for the direct effect of the LWC on RDF, a little decline is observed with increasing the droplet mass loading.

These observations clearly demonstrate that RDF and RRV are intertwined (Perrin and Jonker 2014). The decline in the RDF is caused by the enhancement in RRV via increasing the LWC. In contrast, the RDF grows when the lubrication forces are accounted for. This is because the strong viscous forces reduce the RRV, so that the droplets can stay longer at closer separations.

In Fig. 3, the RDF of settling droplets (right panels) exhibits even more original attributes. When AI is ignored, the RDF grows until $St \approx 1$, followed by a slight decline with St. This trend is also maintained for all LWCs when AI is taken into account. It should be added that clustering of settling droplets strongly varies depending on the LWC. The RDF of interacting droplets in the presence of gravity reveals three important features. Firstly, the RDF continues to grow with droplet inertia (St) when LWC = 3 g/m^3, and flattens or even declines when $St \gtrsim 0.8$. The reduction is more evident at larger LWC values, i.e. 10 and 30 g/m^3. Secondly, the highest RDF is always in systems where lubrication forces are additionally considered. Lastly, at low LWCs, the RDF of interacting droplets both with and without lubrication effects are very close. However, as the LWC increases, the RDF of systems with long-range AI (without lubrication) decreases. This is due to the higher collision rate in such systems (see the corresponding panels in Fig. 4) which prevents clustering. An inverse trend was seen in Fig. 2 for the RRV, which showed an increase in RRV with the LWC. The fluctuations due to droplet AI decorrelates their motion and hence decreases their clustering. The comparison of the RDF data from Table A.3 of Wang et al. (2008) with monodisperse data presented here (mid-right panel) shows a qualitative agreement.

In the next step, we discuss the effect of AI on the dynamic collision kernel. To ensure consistency, the analyzed data were taken from the same simulations used previously to evaluate kinematic statistics. The complete set of results showing the dependence of the dynamic collision kernel on the Stokes number is presented in Fig. 4. As a measure of volumetric collision frequency, the collision kernel is directly proportional to the product of RRV and RDF (at contact). The presented values are normalized by the Kolmogorov microscales of the turbulent flow. The obtained results show that the collision kernels grow monotonically with the inertia of droplets, regardless of the presence of gravity. It should be emphasized, however, that this enhancement is larger for the no-gravity case. The observed increase is due to the decorrelation of the fluid and particle velocities. Such effect is clearly visible in the augmented RRV. This explains why for non-settling droplets, the increasing trends of the collision kernel are similar to those in the RRV. When gravity is not included, the largest collision kernels are for the systems with non-interacting droplets. A lower collision rate is observed when AI, and lubrication effects, are accounted for. Interestingly, these dependencies are reversed for the settling particles. Moreover, the relationship between Γ^{D} and the Stokes number is more sensitive to AI. There is a change in the trend around $St \approx 1$, after which the increase in the collision kernel of the non-interacting droplets saturates due to the decline in RRV. Such flattening is not observed in the Γ^{D} of interacting droplets. Furthermore, the collision kernel reveals a noticeable enhancement as the LWC increases. This analysis clearly demonstrates the importance of AI for both settling and non-settling droplets, especially in systems with high LWCs. Back to the simulations without gravity, we notice that the reduction in Γ^{D} due to AI is of the same order for all the LWCs analyzed here. This is a non-trivial result because RDF and RRV, presented in Figs. 2 and 3, reveal opposite dependencies on the presence of AI. The net effect of these two opposing behaviors results in the reduction of the collision kernel. Finally, it is worth adding that although gravity usually decreases the collision kernel, the velocity disturbances due to droplet AI can augment its value.

The collision efficiency has been quantified and the computed values are presented in Fig. 5. The vertical axes are shown in a logarithmic scale but their ranges are chosen differently for non-settling and settling systems, unlike the plots in previous figures. Outcomes of those numerical experiments allow us to draw the conclusion that the collision efficiency is vitally dependent on gravity. In the no-gravity case, E stays below unity over a

wide range of the Stokes number and LWC values. This means that the Γ^{D} of non-interacting droplets must be consistently larger than interacting ones. The data presented in Fig. 4 (left column) confirm this trend. As mentioned earlier, this is due to the higher relative velocity of no-AI droplets. For systems with a relatively small mass loading, namely having a LWC ≤ 10 g/m^3, the collision efficiency has a characteristic minimum at $St \approx 0.4$. It is worth noting that an analogous minimum also appears when gravity is included. The decreasing trend at low St is in a quantitative agreement with the results of Chen et al. (2018a), who have tabulated collision efficiency of pairs of droplets in flows of various dissipation rates (the data for same-size pairs under $\epsilon = 500$ cm^2/s^3 is shown here).

As the LWC increases, the E of the non-settling droplets becomes less and less dependent on St. However, the results become more sensitive to different AI representations. The key observation concerns simulations with gravity. For large Stokes numbers and significant mass loading (LWC = 30 g/m^3), E can be as high as 3. There are two reasons for such strong enhancement. First, in systems with heavy droplets, disturbance velocity induced by their motion is relatively large and causes an increase in RRV. Second, the clustering of droplets in such systems is more efficient, which is reflected in higher RDF values.

Finally, we make an effort to answer the question that to what extent different representations of AI alter the turbulence enhancement factor (defined in Eq. (17)). The post-processed data from simulations with the settling droplets are shown in Fig. 6. Earlier

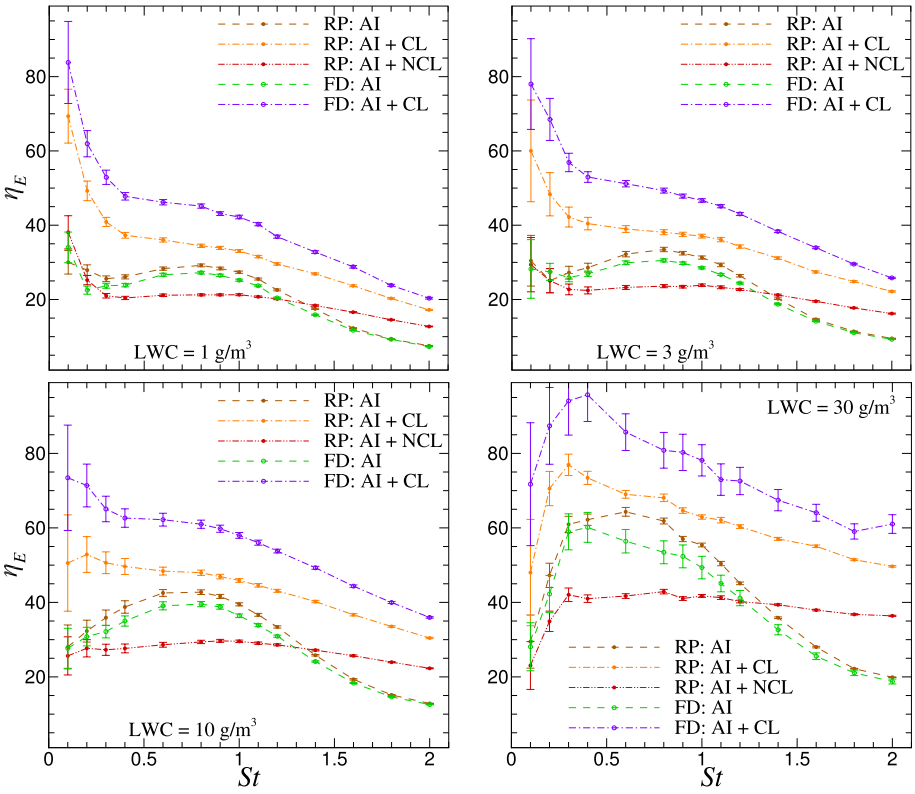

Fig. 6 The turbulence enhancement factor as a function of droplet Stokes number in settling droplet systems

studies on bidisperse droplet systems (Wang et al. 2008; Chen et al. 2018a) have shown a significant enhancement in η_E due to turbulence when $a_2/a_1 \to 1$ (monodisperse) and $a_2/a_1 \to 0$. For the range in between, the enhancement is close to unity. In this study, only monodisperse systems are modeled, so the obtained values (presented in Fig. 6) are relatively large, especially in the range of small Stokes numbers. Noteworthily, in most of the considered cases, for $St \gtrsim 0.8$ the enhancement factor systematically declines, indicating that the importance of turbulence vanishes in comparison with gravity. This is in accordance with the observations of Wang et al. (2008). Furthermore, the enhancement factor grows with the LWC. This growth is directly caused by the disturbances due to droplet AI induced by a greater number of droplets, augmenting the collision kernel. As discussed above, when AI is neglected the collision statistics are not impacted by the LWC.

For low-inertia droplets, there is an increase in η_E with St. This stems from the decline in the turbulence collision efficiency, whereas the still-air gravitational collision efficiency is a monotonically increasing function of St. Such effect is not observed in the cases where lubrication is taken into account. For these cases, the largest enhancement is obtained under the fluid drop (FD) model, followed by a lower η_E under the rigid particle (RP) with a continuum (CL) and then a non-continuum (NCL) representation of lubrication effects. Since the turbulent collision efficiencies of the systems with different lubrication models are very close, these variations are mainly due to the changes in the still-air (gravitational) collision efficiency.

4 Conclusions

The kinematics and dynamics of particle-laden turbulent flows have been investigated by means of hybrid direct numerical simulations together with Lagrangian particle tracking and employing the point-particle approximation. The hybrid approach accounts for particle–particle aerodynamic interaction through the superposition of Stokes disturbances induced by translating particles. The particles were supposed to represent droplets (via water properties) that are typical of atmospherics clouds (via a representative dissipation rate of kinetic energy in turbulent air), yet the results do not lose generality. The simulations were performed both in the absence and presence of gravity covering a wide range of liquid water contents (1–30 g/m^3). Moreover, a detailed comparison was made between assuming the droplets as rigid particles and as fluid drops with internal circulation. In addition, the influence of both continuum and non-continuum models to represent the short-range lubrication effect on the collision statistics was examined. Lastly, the enhancement factor due to turbulence was quantified to illustrate the significance of turbulence in boosting the collision rate relative to that by gravity.

Several conclusions were drawn based on the results from numerical simulations. Considering the aerodynamic interaction is quite important especially when modeling high-LWC systems of droplets that are settling under gravity. Likewise, the lubrication effects significantly change the statistics when considered. In the absence of gravity, there is a noticeable decrease in the RRV and an enhancement in the RDF when the lubrication forces are taken into account. If gravity is included, the influence of AI on RRV strongly depends on the LWC. At large mass loadings, short-range AI forces can more than double the RRV. These effects are reflected in the values of collision kernel and efficiency. For the no-gravity case, the lubrication forces result in a reduction in Γ^{D} such that the collision efficiency is always below unity. In simulations with gravity, these trends are totally

opposite, and both parameters are sensitive to the LWC. The collision efficiency increases with LWC to values much greater than unity. In this context, it is also worth recalling the properties of the turbulence enhancement factor. This parameter decreases with the droplet inertia, suggesting that the enhancement in collision rate due to turbulence is being taken over by gravity.

The statistics are very close whether the continuum or the non-continuum representation of lubrication is employed. Similarly, utilizing the fluid drop model, as an alternative to the rigid particle assumption, does not have substantial influence on the collision statistics. These two observations imply that for medium-sized droplets ($\approx$ 10–60 μm) that have a large viscosity ratio (e.g. water in air), the models are sufficiently accurate when the droplets are assumed to be rigid particles and when the droplet AI employs a lubrication representation based on the continuum assumption $Kn \to 0$.

The results reported here pave the way for a more realistic modeling of particle-laden turbulent flows. However, further work is warranted to explore the effect of AI in bi- or polydisperse systems. It would also be interesting to develop a more physical approach for treating droplets after collisions. Moreover, to represent cloud processes more faithfully, future experiments should be performed using larger domains.

Acknowledgements We would like to express our sincere gratitude to Alexander Z. Zinchenko (University of Colorado Boulder) for sharing with us the Fortran implementation for computing AI between fluid drops and many useful suggestions and remarks. We are also genuinely thankful for the valuable comments we have received from Donald L. Koch and Anubhab Roy (Cornell University). With their help, we were able to solve several problems encountered during the implementation of the algorithm for computing non-continuum lubrication forces.

Author Contributions AA: Investigation, Methodology, Writing—original draft, Software, Validation; AM: Writing—review & editing, Investigation; BR: Conceptualization, Writing—review & editing, Data curation, Supervision.

Funding This study was financially supported by the National Science Center of Poland under the grant 2018/30/Q/ST8/00341. *Computational Resources* We wish to thank both the Institute of Meteorology and Water Management – National Research Institute (IMGW–PIB), and the Interdisciplinary Center for Mathematical and Computational Modeling at the University of Warsaw (ICM–UW) for providing the computational resources under the grants G87-1145 and G92-1450.

Code Availability The code for computing AI is available in github.com/aababaei/Two-Sphere-Interaction. The resistance functions were taken from the research web-page of David Jeffrey: www.uwo.ca/apmaths/faculty/jeffrey/research/Resistance.html.

Declarations

Competing Interests The authors declare no competing interests.

Ethics Approval The authors comply with the ethical standards.

Informed Consent Informed consent was obtained from all authors before submitting this study.

References

Ababaei, A., Rosa, B.: Collision efficiency of cloud droplets in quiescent air considering lubrication interactions, mobility of interfaces, and noncontinuum molecular effects. Phys. Rev. Fluids **8**(1), 014–102 (2023)

Ababaei, A., Rosa, B., Pozorski, J., et al.: On the effect of lubrication forces on the collision statistics of cloud droplets in homogeneous isotropic turbulence. J. Fluid Mech. **918**, A22 (2021)

Akiki, G., Jackson, T.L., Balachandar, S.: Pairwise interaction extended point-particle model for a random array of monodisperse spheres. J. Fluid Mech. **813**, 882–928 (2017)

Akiki, G., Moore, W.C., Balachandar, S.: Pairwise-interaction extended point-particle model for particle-laden flows. J. Comput. Phys. **351**, 329–357 (2017)

Ayala, O., Wang, L.P.: Parallel implementation and scalability analysis of 3D fast Fourier transform using 2D domain decomposition. Parallel Comput. **39**(1), 58–77 (2013)

Ayala, O., Grabowski, W.W., Wang, L.P.: A hybrid approach for simulating turbulent collisions of hydrodynamically-interacting particles. J. Comput. Phys. **225**(1), 51–73 (2007)

Ayala, O., Rosa, B., Wang, L.P., et al.: Effects of turbulence on the geometric collision rate of sedimenting droplets. Part 1 .Results from direct numerical simulation. New J. Phys. **10**, 075015 (2008)

Ayala, O., Parishani, H., Chen, L., et al.: DNS of hydrodynamically interacting droplets in turbulent clouds: Parallel implementation and scalability analysis using 2D domain decomposition. Comput. Phys. Commun. **185**(12), 3269–3290 (2014)

Balachandar, S., Maxey, M.R.: Methods for evaluating fluid velocities in spectral simulations of turbulence. J. Comput. Phys. **83**(1), 96–125 (1989)

Batchelor, C.K., Batchelor, G.K.: An introduction to fluid dynamics. Cambridge University Press, Cambridge (2000)

Beard, K.V., Ochs, H.T.: Warm-rain initiation: An overview of microphysical mechanisms. J. Appl. Meteorol. **32**(4), 608–625 (1993)

Beshkov, V.N., Radoev, B.P., Ivanov, I.B.: Slow motion of two droplets and a droplet towards a fluid or solid interface. Int. J. Multiph. Flow **4**(5–6), 563–570 (1978)

Bragg, A.D., Hammond, A.L., Dhariwal, R., et al.: Hydrodynamic interactions and extreme particle clustering in turbulence. J. Fluid Mech. **933**, A31 (2022)

Brunk, B.K., Koch, D.L., Lion, L.W.: Turbulent coagulation of colloidal particles. J. Fluid Mech. **364**, 81–113 (1998)

Chen, S., Yau, M.K., Bartello, P.: Turbulence effects of collision efficiency and broadening of droplet size distribution in cumulus clouds. J. Atmos. Sci. **75**(1), 203–217 (2018)

Chen, S., Yau, M.K., Bartello, P., et al.: Bridging the condensation-collision size gap: A direct numerical simulation of continuous droplet growth in turbulent clouds. Atmos. Chem. Phys. **18**, 7251–7262 (2018)

Chun, J., Koch, D.L.: Coagulation of monodisperse aerosol particles by isotropic turbulence. Phys. Fluids **17**(2), 027102 (2005)

Dávila, J., Hunt, J.C.R.: Settling of small particles near vortices and in turbulence. J. Fluid Mech. **440**, 117–145 (2001)

Davis, M.H., Sartor, J.D.: Theoretical collision efficiencies for small cloud droplets in Stokes flow. Nature **215**(5108), 1371–1372 (1967)

Davis, R.H.: The rate of coagulation of a dilute polydisperse system of sedimenting spheres. J. Fluid Mech. **145**, 179–199 (1984)

Davis, R.H., Schonberg, J.A., Rallison, J.M.: The lubrication force between two viscous drops. Phys. Fluids A: Fluid Dyn. **1**(1), 77–81 (1989)

de Almeida, F.C.: The collisional problem of cloud droplets moving in a turbulent environment-Part II: Turbulent collision efficiencies. J. Atmos. Sci. **36**(8), 1564–1576 (1979)

Dhanasekaran, J., Roy, A., Koch, D.L.: Collision rate of bidisperse, hydrodynamically interacting spheres settling in a turbulent flow. J. Fluid Mech. **912**, A5 (2021)

Dhanasekaran, J., Roy, A., Koch, D.L.: Collision rate of bidisperse spheres settling in a compressional noncontinuum gas flow. J. Fluid Mech. **910**, A10 (2021)

Durlofsky, L., Brady, J.F., Bossis, G.: Dynamic simulation of hydrodynamically interacting particles. J. Fluid Mech. **180**, 21–49 (1987)

Falkovich, G., Pumir, A.: Sling effect in collisions of water droplets in turbulent clouds. J. Atmos. Sci. **64**(12), 4497–4505 (2007)

Fornari, W., Picano, F., Sardina, G., et al.: Reduced particle settling speed in turbulence. J. Fluid Mech. **808**, 153–167 (2016)

Fung, J.C.H.: Effect of nonlinear drag on the settling velocity of particles in homogeneous isotropic turbulence. J. Geophys. Res. Oceans **103**(C12), 27905–27917 (1998)
Good, G.H., Ireland, P.J., Bewley, G.P., et al.: Settling regimes of inertial particles in isotropic turbulence. J. Fluid Mech. **759**, R3 (2014)
Grabowski, W.W., Wang, L.P.: Growth of cloud droplets in a turbulent environment. Annual Rev. Fluid Mech. **45**(1), 293–324 (2013)
Grashchenkov, S.I.: The effect of slip on the motion of two droplets and of a droplet close to a plane surface of a liquid. Aerosol Sci. Technol. **25**(2), 101–112 (1996)
Grover, S.N., Pruppacher, H.R.: The effect of vertical turbulent fluctuations in the atmosphere on the collection of aerosol particles by cloud drops. J. Atmos. Sci. **42**(21), 2305–2318 (1985)
Haber, S., Hetsroni, G., Solan, A.: On the low Reynolds number motion of two droplets. Int. J. Multiph. Flow **1**(1), 57–71 (1973)
Hadamard, J.S.: Mouvement permanent lent d'une sphère liquide et visqueuse dans un liquide visqueux. Comptes Rendus de l'Acadèmie des Sci. **152**, 1735–1738 (1911)
Hall, W.D.: A detailed microphysical model within a two-dimensional dynamic framework: Model description and preliminary results. J. Atmos. Sci. **37**(11), 2486–2507 (1980)
Hocking, L.M.: The collision efficiency of small drops. Q. J. R. Meteorol. Soc. **85**(363), 44–50 (1959)
Hocking, L.M., Jonas, P.R.: The collision efficiency of small drops. Q. J. R. Meteorol. Soc. **96**(410), 722–729 (1970)
Ireland, P.J., Bragg, A.D., Collins, L.R.: The effect of Reynolds number on inertial particle dynamics in isotropic turbulence. Part 2. Simulations with gravitational effects. J. Fluid Mech. **796**, 659–711 (2016)
Jeffrey, D.J., Onishi, Y.: Calculation of the resistance and mobility functions for two unequal rigid spheres in low-Reynolds-number flow. J. Fluid Mech. **139**, 261–290 (1984)
Kim S, Karrila SJ (2013) Microhydrodynamics: principles and selected applications. Courier Corporation
Klett, J.D., Davis, M.H.: Theoretical collision efficiencies of cloud droplets at small Reynolds numbers. J. Atmos. Sci. **30**(1), 107–117 (1973)
Koziol, A.S., Leighton, H.G.: The effect of turbulence on the collision rates of small cloud drops. J. Atmos. Sci. **53**, 1910–1920 (1996)
Lefebvre-Lepot, A., Merlet, B., Nguyen, T.N.: An accurate method to include lubrication forces in numerical simulations of dense Stokesian suspensions. J. Fluid Mech. **769**, 369–386 (2015)
Li Sing How, M., Koch, D.L., Collins, L.R.: Non-continuum tangential lubrication gas flow between two spheres. J. Fluid Mech. **920**, A2 (2021)
Magnusson, G., Dubey, A., Kearney, R., et al.: Collisions of micron-sized charged water droplets in still air. Phys. Rev. Fluids **7**(4), 043601 (2022)
Maude, A.D.: End effects in a falling-sphere viscometer. Br. J. Appl. Phys. **12**(6), 293–295 (1961)
Maxey, M.R.: The gravitational settling of aerosol particles in homogeneous turbulence and random flow fields. J. Fluid Mech. **174**, 441–465 (1987)
Maxey, M.R.: The motion of small spherical particles in a cellular flow field. Phys. Fluids **30**(7), 1915–1928 (1987)
Maxey, M.R., Corrsin, S.: Gravitational settling of aerosol particles in randomly oriented cellular flow fields. J. Atmos. Sci. **43**(11), 1112–1134 (1986)
Maxey, M.R., Riley, J.J.: Equation of motion for a small rigid sphere in a nonuniform flow. Phys. Fluids **26**(4), 883–889 (1983)
Nielsen, P.: Turbulence effects on the settling of suspended particles. J. Sediment. Res. **63**(5), 835–838 (1993)
O'Neill, M.E., Majumdar, S.R.: Asymmetrical slow viscous fluid motions caused by the translation or rotation of two spheres. Part I: The determination of exact solutions for any values of the ratio of radii and separation parameters. Zeitschrift für Angewandte Mathematik und Physik **21**(2), 164–179 (1970)
Onishi, R., Takahashi, K., Vassilicos, J.C.: An efficient parallel simulation of interacting inertial particles in homogeneous isotropic turbulence. J. Comput. Phys. **242**, 809–827 (2013)
Orszag, S.A., Patterson, G.S.: Numerical simulation of three-dimensional homogeneous isotropic turbulence. Phys. Rev. Lett. **28**(2), 76 (1972)
Patra, P., Roy, A.: Brownian coagulation of like-charged aerosol particles. Phys. Rev. Fluids **7**(6), 064308 (2022)
Patra, P., Koch, D.L., Roy, A.: Collision efficiency of non-brownian spheres in a simple shear flow-the role of non-continuum hydrodynamic interactions. J. Fluid Mech. **950**, A18 (2022)
Pawar, S., Padding, J., Deen, N., et al.: Numerical and experimental investigation of induced flow and droplet-droplet interactions in a liquid spray. Chem. Eng. Sci. **138**, 17–30 (2015)
Perrin, V.E., Jonker, H.J.J.: Preferred location of droplet collisions in turbulent flows. Phys. Rev. E **89**(3), 033005 (2014)

Pinsky, M., Khain, A., Shapiro, M.: Collisions of small drops in a turbulent flow. Part I: Collision efficiency. Problem formulation and preliminary results. J. Atmos. Sci. **56**(15), 2585–2600 (1999)
Pinsky, M., Khain, A., Shapiro, M.: Collision efficiency of drops in a wide range of Reynolds numbers: Effects of pressure on spectrum evolution. J. Atmos. Sci. **58**(7), 742–764 (2001)
Pinsky, M., Khain, A., Shapiro, M.: Collisions of cloud droplets in a turbulent flow. Part IV: Droplet hydrodynamic interaction. J. Atmos. Sci. **64**(7), 2462–2482 (2007)
Press, W.H., Teukolsky, S.A., Flannery, B.P., et al.: Numerical recipes in Fortran 77: The art of scientific computing. Cambridge University Press, Cambridge (1992)
Rafidi, N., Brogaard, F., Chen, L., et al.: CFD and experimental studies on capture of fine particles by liquid droplets in open spray towers. Sustain. Environ. Res. **28**(6), 382–388 (2018)
Reade, W.C., Collins, L.R.: Effect of preferential concentration on turbulent collision rates. Phys. Fluids **12**(10), 2530–2540 (2000)
Rosa, B., Wang, L.P., Maxey, M.R., et al.: An accurate and efficient method for treating aerodynamic interactions of cloud droplets. J. Comput. Phys. **230**(22), 8109–8133 (2011)
Rosa, B., Parishani, H., Ayala, O., et al.: Kinematic and dynamic collision statistics of cloud droplets from high-resolution simulations. New J. Phys. **15**(4), 045032 (2013)
Rosa, B., Parishani, H., Ayala, O., et al.: Settling velocity of small inertial particles in homogeneous isotropic turbulence from high-resolution DNS. Int. J. Multiph. Flow **83**, 217–231 (2016)
Rother, M.A., Stark, J.K., Davis, R.: Gravitational collision efficiencies of small viscous drops at finite Stokes numbers and low Reynolds numbers. Int. J. Multiph. Flow **146**(103), 876 (2022)
Rybczyński W (1911) Über die fortschreitende bewegung einer flüssigen kugel in einem zähen medium. Bulletin International de L'Acadèmie des Science de Cracovie A:40–46
Saffman, P.G.F., Turner, J.S.: On the collision of drops in turbulent clouds. J. Fluid Mech. **1**(1), 16–30 (1956)
Sangani, A.S., Mo, G.: Inclusion of lubrication forces in dynamic simulations. Phys. Fluids **6**(5), 1653–1662 (1994)
Sangani, A.S., Mo, G.: An O(N) algorithm for stokes and laplace interactions of particles. Phys. Fluids **8**(8), 1990–2010 (1996)
Shafrir, U., Neiburger, M.: Collision efficiencies of two spheres falling in a viscous medium. J. Geophys. Res. **68**(13), 4141–4147 (1963)
Squires, K.D., Eaton, J.K.: Particle response and turbulence modification in isotropic turbulence. Phys. Fluids **2**(7), 1191–1203 (1990)
Stimson, M., Jeffery, G.B.: The motion of two spheres in a viscous fluid. Proc. R. Soc. London **111**(757), 110–116 (1926)
Sullivan, N.P., Mahalingam, S., Kerr, R.M.: Deterministic forcing of homogeneous, isotropic turbulence. Phys. Fluids **6**(4), 1612–1614 (1994)
Sundaram, S., Collins, L.R.: Collision statistics in an isotropic particle-laden turbulent suspension. Part 1. Direct numerical simulations. J. Fluid Mech. **335**, 75–109 (1997)
Sundararajakumar, R.R., Koch, D.L.: Non-continuum lubrication flows between particles colliding in a gas. J. Fluid Mech. **313**, 283–308 (1996)
Tooby, P.F., Wick, G.L., Isaacs, J.D.: The motion of a small sphere in a rotating velocity field: A possible mechanism for suspending particles in turbulence. J. Geophys. Res. **82**(15), 2096–2100 (1977)
Torres, C.E., Parishani, H., Ayala, O., et al.: Analysis and parallel implementation of a forced N-body problem. J. Comput. Phys. **245**, 235–258 (2013)
Voßkuhle, M., Pumir, A., Lévêque, E., et al.: Prevalence of the sling effect for enhancing collision rates in turbulent suspensions. J. Fluid Mech. **749**, 841–852 (2014)
Wacholder, E., Weihs, D.: Slow motion of a fluid sphere in the vicinity of another sphere or a plane boundary. Chem. Eng. Sci. **27**(10), 1817–1828 (1972)
Wang, L.P., Maxey, M.R.: Settling velocity and concentration distribution of heavy particles in homogeneous isotropic turbulence. J. Fluid Mech. **256**, 27–68 (1993)
Wang, L.P., Wexler, A.S., Zhou, Y.: On the collision rate of small particles in isotropic turbulence. i. zero-inertia case. Phys. Fluids **10**, 266–276 (1998)
Wang, L.P., Wexler, A.S., Zhou, Y.: Statistical mechanical descriptions of turbulent coagulation. Phys. Fluids **10**(10), 2647–2651 (1998)
Wang, L.P., Wexler, A.S., Zhou, Y.: Statistical mechanical description and modelling of turbulent collision of inertial particles. J. Fluid Mech. **415**, 117–153 (2000)
Wang, L.P., Ayala, O., Grabowski, W.W.: Improved formulations of the superposition method. J. Atmos. Sci. **62**(4), 1255–1266 (2005)

Wang, L.P., Ayala, O., Kasprzak, S.E., et al.: Theoretical formulation of collision rate and collision efficiency of hydrodynamically interacting cloud droplets in turbulent atmosphere. J. Atmos. Sci. **62**(7), 2433–2450 (2005)
Wang, L.P., Ayala, O., Xue, Y.: Reconciling the cylindrical formulation with the spherical formulation in the kinematic descriptions of collision kernel. Phys. Fluids **17**(6), 067103 (2005)
Wang, L.P., Ayala, O., Grabowski, W.W.: Effects of aerodynamic interactions on the motion of heavy particles in a bidisperse suspension. J. Turbul. **8**, N25 (2007)
Wang, L.P., Ayala, O., Rosa, B., et al.: Turbulent collision efficiency of heavy particles relevant to cloud droplets. New J. Phys. **10**(7), 075013 (2008)
Wang, L.P., Rosa, B., Gao, H., et al.: Turbulent collision of inertial particles: point-particle based, hybrid simulations and beyond. Int. J. Multiph. Flow **35**(9), 854–867 (2009)
Woittiez, E.J.P., Jonker, H.J.J., Portela, L.M.: On the combined effects of turbulence and gravity on droplet collisions in clouds: A numerical study. J. Atmos. Sci. **66**(7), 1926–1943 (2009)
Yavuz, M.A., Kunnen, R.P.J., Van Heijst, G.J.F., et al.: Extreme small-scale clustering of droplets in turbulence driven by hydrodynamic interactions. Phys. Rev. Lett. **120**(24), 244504 (2018)
Zhou, Y., Wexler, A.S., Wang, L.P.: On the collision rate of small particles in isotropic turbulence. ii. Finite inertia case. Phys. Fluids **10**, 1206–1216 (1998)
Zhou, Y., Wexler, A.S., Wang, L.P.: Modelling turbulent collision of bidisperse inertial particles. J. Fluid Mech. **433**, 77–104 (2001)
Zinchenko, A.Z.: Calculation of hydrodynamic interaction between drops at low Reynolds numbers. J. Appl. Math. Mech. **42**(5), 1046–1051 (1978)
Zinchenko, A.Z.: The slow asymmetric motion of two drops in a viscous medium. J. Appl. Math. Mech. **44**(1), 30–37 (1980)